ELSEVIER

NeuroImage

www.elsevier.com/locate/ynimg
NeuroImage 26 (2005) 1009 – 1018

Automated brain tissue assessment in the elderly and demented population: Construction and validation of a sub-volume probabilistic brain atlas

Michael S. Mega,[a,*] Ivo D. Dinov,[b,d,e] John C. Mazziotta,[b,d,f] Mario Manese,[b,d] Paul M. Thompson,[b,d] Chris Lindshield,[b,d] Jacob Moussai,[b,d] Nah Tran,[b,d] Kirsten Olsen,[b,d] Chris I. Zoumalan,[b,d] Roger P. Woods,[b,c,d] and Arthur W. Toga[b,c,d]

[a]*Alzheimer's Disease Center, Providence Health System, 10150 SE 32nd Avenue, Portland, OR 97222, USA*
[b]*Laboratory of Neuro Imaging, David Geffen School of Medicine at UCLA, Los Angeles, CA 90095, USA*
[c]*Ahmanson-Lovelace Brain Mapping Center, David Geffen School of Medicine at UCLA, Los Angeles, CA 90095, USA*
[d]*Departments of Neurology, David Geffen School of Medicine at UCLA, Los Angeles, CA 90095, USA*
[e]*Statistics, David Geffen School of Medicine at UCLA, Los Angeles, CA 90095, USA*
[f]*Radiology, Pharmacology, and Neuropsychiatric Institute, David Geffen School of Medicine at UCLA, Los Angeles, CA 90095, USA*

Received 24 June 2004; revised 8 March 2005; accepted 16 March 2005
Available online 23 May 2005

Objectives: To develop an automated imaging assessment tool that accommodates the anatomic variability of the elderly and demented population as well as the registration errors occurring during spatial normalization. Methods: 20 subjects with Alzheimer's disease (AD), mild cognitive impairment, or normal cognition underwent MRI brain imaging and had their 3D volumetric datasets manually partitioned into 68 regions of interest (ROI) termed sub-volumes. Gray matter (GM), white matter (WM), and cerebral spinal fluid (CSF) voxel counts were then made in the subject's native space for comparison against automated volumetric measures within three sub-volume probabilistic atlas (SVPA) models. The three SVPAs were constructed using 12 parameter affine (12 p), 2nd order (2nd), and 6th order (6th) transforms derived from registering the manually partitioned scans into a Talairach compatible AD population-based target. The three SVPA automated measures were compared to the manually derived measures in the 20 subjects' native space with a "jack-knife" procedure in which each subject was assessed by an SVPA they did not contribute toward constructing. Results: The mean left and right GM ratio (GM ratio = [GM + CSF] / CSF) "*r* values" for the 3 SVPAs compared to the manually derived ratios across the 68 ROIs were 0.85 for the 12p SVPA, 0.88 for the 2nd SVPA, and 0.89 for the 6th SVPA. The mean left and right WM ratio (WM ratio = [WM + CSF] / CSF) "*r* values" for the 3 SVPAs being 0.84 for the 12p SVPA, 0.86 for the 2nd SVPA, and 0.88 for the 6th SVPA. Conclusion: We have constructed, from an elderly and demented cohort, an automated brain volumetric tool that has excellent accuracy compared to a manual gold standard and is capable of regional hypothesis testing and individual patient assessment compared to a population.

Keywords: Alzheimer's disease; MRI; Brain mapping; Neuroimaging

Introduction

Neuroimaging in aging and dementia is now at a critical turning point. The accumulation of findings since the first functional and structural studies of dementia has produced sufficient observational data to bring the field to the threshold of a new challenge—the identification of incipient Alzheimer's disease in the individual. Results from past observational studies in patients, and elderly normal subjects, enable us to test the *prospective* sensitivity and specificity of a few discrete regional abnormalities in correctly identifying incipient AD. Unfortunately, no single institution can easily amass enough longitudinal population data to power the analysis of an individuals' likelihood of having incipient AD. The urgency in meeting the challenge of identifying the individual, who may not even have cognitive complaints, prior to developing dementia symptoms is now apparent given our society's changing demographics and the emergence of disease modifying treatments. A major impediment to meeting this challenge is the development of an imaging assessment tool that can be universally applied and possess sufficient power to identify an individual's disease risk compared to an unaffected population.

Four difficulties face the development of this imaging technique: (1) the assessment tool must control for anatomic variability and

* Corresponding author. Fax: +1 503 513 8501.
E-mail address: michael.mega@providence.org (M.S. Mega).
Available online on ScienceDirect (www.sciencedirect.com).

1053-8119/$ - see front matter © 2005 Elsevier Inc. All rights reserved.
doi:10.1016/j.neuroimage.2005.03.031

registration errors produced when comparing datasets in a common co-ordinate system; (2) the tool must allow for regionally testable hypotheses; (3) to ensure inter-center application, the imaging tool must be automated, freely available, and not require extensive computer resources; and (4) the tool should accommodate growth in its population data. This study demonstrates a candidate imaging assessment tool that addresses the above difficulties.

Methods

Overview

To determine the best registration algorithm to a common target space (a population-based atlas designed to accommodate the elderly and demented brain previously described) (Thompson et al., 2001b), we test three polynomial registration approaches into our atlas target using Automated Image Registration (AIR) (Woods et al., 1998): 12 parameter affine (12 p), 30 parameter 2nd order warp (2nd), or 168 parameter 6th order warp (6th) using 3 dimensional magnetic resonance imaging (3D MRI) data from 20 subjects. Regional native space tissue counts derived from manual outlines served as the gold standard to determine the best overall accuracy of automated gray matter (GM), white matter (WM), and cerebral spinal fluid (CSF) voxel counts derived from the three transforms. Here, we define a *sub-volume* as a region of interest (ROI) within the target atlas; a *probability gradient* is the three-dimensional (3D) probability distribution across atlas voxels of being within a given ROI. Thus, some voxels in, for example, the thalamic sub-volume of the atlas, will always contain thalamic tissue in any dataset registered to the atlas, while other atlas thalamic voxels will have a 75%, 50%, 25%, (etc., . . .) chance of localizing the thalamus in a scan registered to the atlas target. Regional sub-volume probability gradients produced within the atlas target space from the three registration approaches are constructed by projecting the manual outlines down the three registration matrices. Thus, three sub-volume probabilistic atlas (SVPA) models are constructed for use as automated tissue counters. The counts obtained with these three SVPAs are then compared to the manual "gold standard" counts to determine their best accuracy.

Subjects

The study group consisted of 20 individuals who presented to the University of California Los Angeles Alzheimer's Disease Research Center, met all study criteria (below), and agreed to scanning after signing an informed consent approved by the Human Subjects Protection Committee. This study included 6 patients with moderate Alzheimer's Disease (AD) and 7 patients with mild disease, all diagnosed according to National Institute of Neurological and Communicative Disorders and Stroke/Alzheimer's Disease and Related Disorders Association (NINCDS/ADRDA) criteria for probable AD (McKhann et al., 1984), 4 patients with Mild Cognitive Impairment (MCI) meeting criteria described by Petersen et al. (1999), and 3 normal elderly subjects enrolled from a population of patient caregivers. We chose a distribution of mild to moderate AD patients, MCI, and controls to extend the application of the SVPA across the population spectrum seen in most clinical research settings. Inclusion criteria included no history of psychiatric disorder in all subjects, or non-AD neurological illness in the AD patients, being sufficiently proficient in English to perform clinical evaluation and age 60 or greater. Exclusion criteria included: all individuals with an abnormal structural imaging study of the brain including cerebral vascular disease, a current or recent psychiatric illness (i.e., affective disorders, psychosis); significant, uncontrolled systemic illness (i.e., chronic renal failure, chronic liver disease, poorly

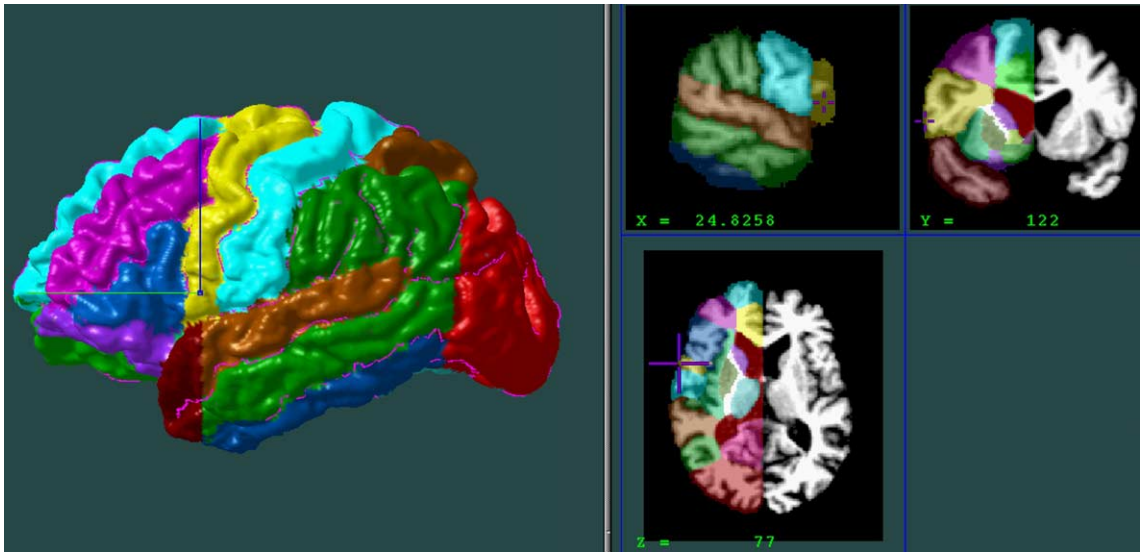

Fig. 1. Volumertric ROIs are manually constructed with the aid of the 3D viewing windows linked to the surface reconstruction available with the Display software package. This ensures that the outliner is able to accurately identify the deep brain anatomy on the slice viewer by receiving visually registered feedback from the surface model (major and minor sulci, outlined in red on the surface model, also can be texture-mapped to the slice windows on the right). Note that the underlying white matter has no distinct landmarks to separate the various cortical ROIs, thus a "spokes-of-the-wheel" approach was used (see for example the coronal view, top right, where the "wheel's hub" is at the dorsolateral tip of the frontal horn of the lateral ventricle) to form a fixed geometry initially created in the atlas space and then projected into each subject's native space via a 9-parameter transform which served as the beginning ROI template for manual refinement guided by each subjects unique cortical anatomy.

controlled diabetes hypertension or congestive heart failure); a history of alcoholism or substance abuse within the past year. Severity of the cognitive deficit was measured in all subjects using the Mini Mental State Exam (MMSE) (Folstein et al., 1975) revealed an average score for the group of 23 (SD 5.39); moderate AD patients scored between 15–19 with mild patient scoring between 20–25. There were a total of 9 females and 11 males, an average age of 76.1 (SD 6.36), and average educational level of 15.6 (SD 2.75).

Scanning protocol

All scans were derived from a GE 1.5 T scanner with the following protocol: coronal 3D volumetric spoiled gradient echo, flip angle 25, TE = minimum FULL, TR = minimum, FOV = 22 cm × 16.5 cm, 124 slices at 1.6 mm/slice, matrix 256 × 192, phase FOV (rectangular FOV), ±10 kHz BW.

Image processing

All scans were transferred from archived digital sources in 16 bit format and manually edited to remove the skull and scalp taking particular caution to preserve the sulcal and subdural CSF. A binary brain mask was then created from the manually edited file and used in a radio frequency bias field correction algorithm using a histogram spline sharpening method (Sled et al., 1998) to eliminate intensity drifts attributable to scanner field inhomogeneity. After inhomogeneity correction, a supervised tissue classifier generated detailed maps of GM, WM, and CSF in the subjects' native space. Briefly, 120 samples of each tissue class were interactively tagged to compute the parameters of a Gaussian mixture distribution that reflects statistical variability in the intensity of each tissue type (Zijdenbos and Dawant, 1994). A nearest neighbor tissue classifier assigned each image voxel to a particular tissue class (GM, WM, or CSF) or to a background class (representing extra-cerebral voxels in the image). The inter-rater and intra-rater reliability of this protocol, and its robustness to changes in image acquisition parameters, have been described previously (Sowell et al., 1999). Gray and white matter maps were retained for subsequent analysis. Native space, skull-stripped, inhomogeneity corrected images were then registered to the standard 3D stereotaxic atlas space (Thompson et al., 2001b) using AIR (Woods et al., 1998) to produce three registration matrices: 12 parameter affine (12 p), 30 parameter 2nd order warp (2nd order), or 168 parameter 6th order warp (6th order) using the standard deviation of ratio images as the cost function.

Regions of interest (ROI) construction

To aid manual ROI construction, a surface model of each subject's cortex was automatically extracted (MacDonald et al., 2000) as previously described (Thompson et al., 2001a). A mesh-like surface is deformed to fit the brain-CSF tissue intensity value of each skull-stripped image volume. The cortical surface software was modified to permit high-resolution extraction of both the lateral and medial hemispheric surfaces, aiding ROI volumetric construction on orthogonal image slices. The following landmarks were outlined on each dataset: the Sylvian fissure; central, precentral, and postcentral sulci; superior temporal sulcus (STS) main body, STS ascending and posterior branches, and primary and secondary intermediate sulci; inferior temporal, superior and inferior frontal, intraparietal, transverse occipital, olfactory, occipitotemporal, collateral, callosal sulcus, and inferior callosal border; the paracentral, anterior, and posterior cingulate and the outer segment of double parallel cingulate sulci (when present) (Ono et al., 1990); the superior and inferior rostral, parieto-occipital, anterior and posterior calcarine, and subparietal sulci. This protocol is available on the Internet (Hayashi et al., 2002; Sowell et al., 2000) and has known inter-rater and intra-rater reliability, as previously reported (Sowell et al., 2001).

In addition to contouring the major and minor sulci, a set of six midline landmark curves bordering the longitudinal fissure was outlined in each hemisphere to establish limits to aid dividing the brain ROI into left and right. Spatially registered gray scale image volumes in the three orthogonal coronal, axial, and sagittal planes (available for simultaneous viewing with the 3D surface model in the Display software package run on the McIntosh OS X platform available at: http://www.bic.mni.mcgill.ca/software/Display/Display.html) were manually segmented into 34 volumetric ROI for each subject's left and right hemisphere (see Fig. 1 and Table 1). All surface and deep brain landmarks were defined according to detailed anatomical protocols (Hayashi et al., 2002; Leonard, 1996; Ono et al., 1990; Sowell et al., 2000, 2001; Steinmetz et al., 1990) and atlasing methods (Amunts et al., 2000; Chiavaras et al., 2001; Crespo-Facorro et al., 1999; Geyer et al., 2000; Kim et al., 2000; Sastre-Janer et al., 1998; White et al., 1997). Extension of the gyral ROI into the underlying WM was accomplished by a "spokes-of-the wheel" technique (see Fig. 1)

Table 1
Regions constructed in the three sub-volume probabilistic atlases (SVPAs) associated with their numerical labels shown in the graphs in Figs. 2 and 3

Region	Label
Cerebellum	1
Occipital	2
Superior parietal	3
Inferior parietal	4
Posterior cingulate	5
Superior temporal	6
Middle temporal	7
Inferior temporal	8
Anterior parahippocampal	9
Hippocampus	10
Amygdala	11
Temporal pole	12
Posterior parahippocampal	13
Caudal anterior cingulate	14
Rostral anterior cingulate	15
Sub-callosal frontal	16
Medial orbital frontal	17
Lateral orbital frontal	18
Inferior frontal	19
Middle frontal	20
Superior frontal	21
Pre-central	22
Post-central	23
Insula	24
Ventricles	25
Substantia nigra	26
Midbrain	27
Pons	28
Medulla	29
Basal medial diencephalon	30
Thalamus	31
Nucleus accumbens	32
Lenticular nucleus	33
Caudate nucleus	34

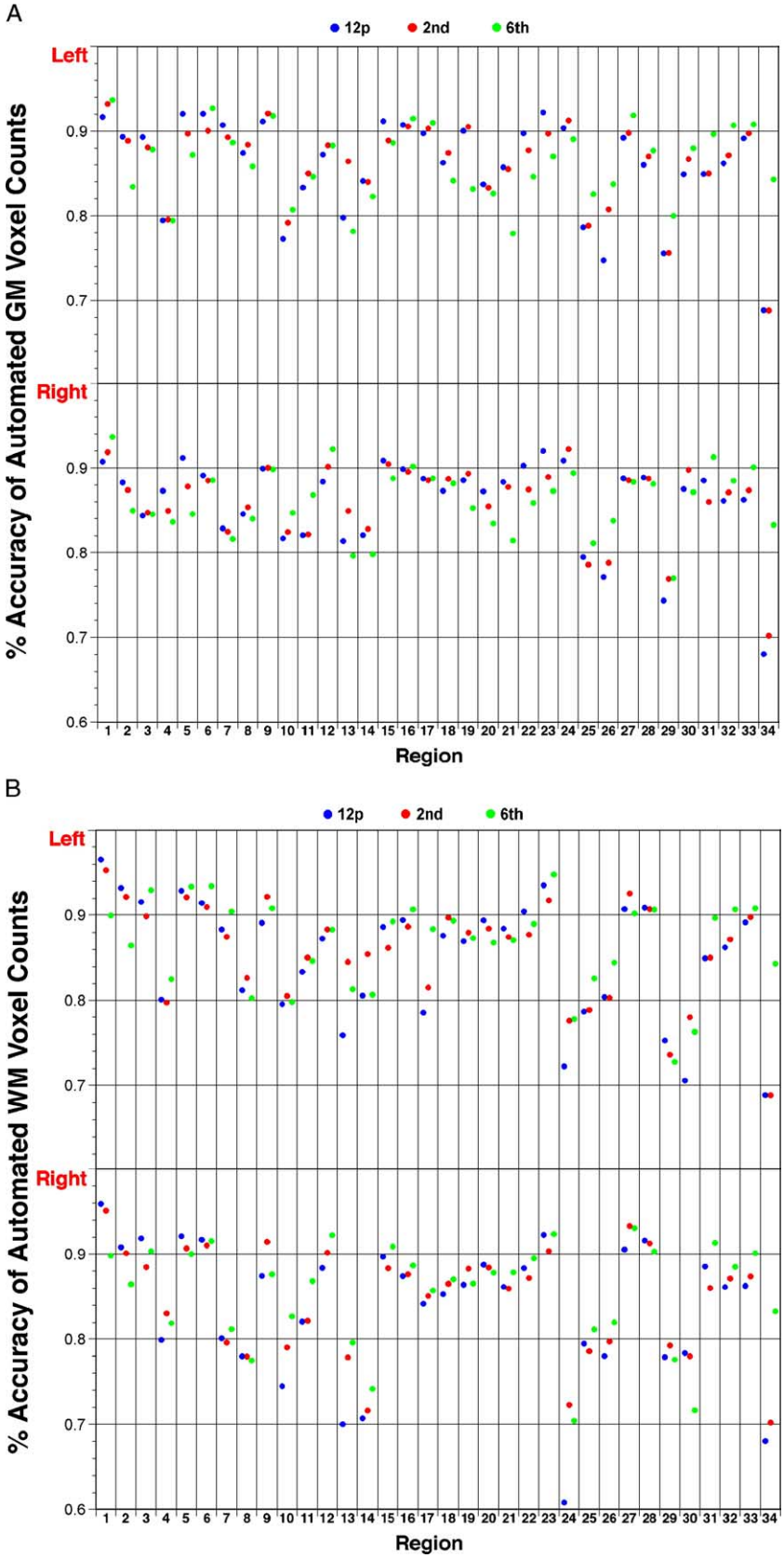

Fig. 2. (A–C) Percent accuracy for the absolute gray matter (A), white matter (B), and cerebral spinal fluid (CSF) counts (C) across all sub-volumes constructed using three different alignments to the population-based target atlas: 12 parameter affine, 2nd order warp, and 6th order warp (see Table 1 for the regions studied).

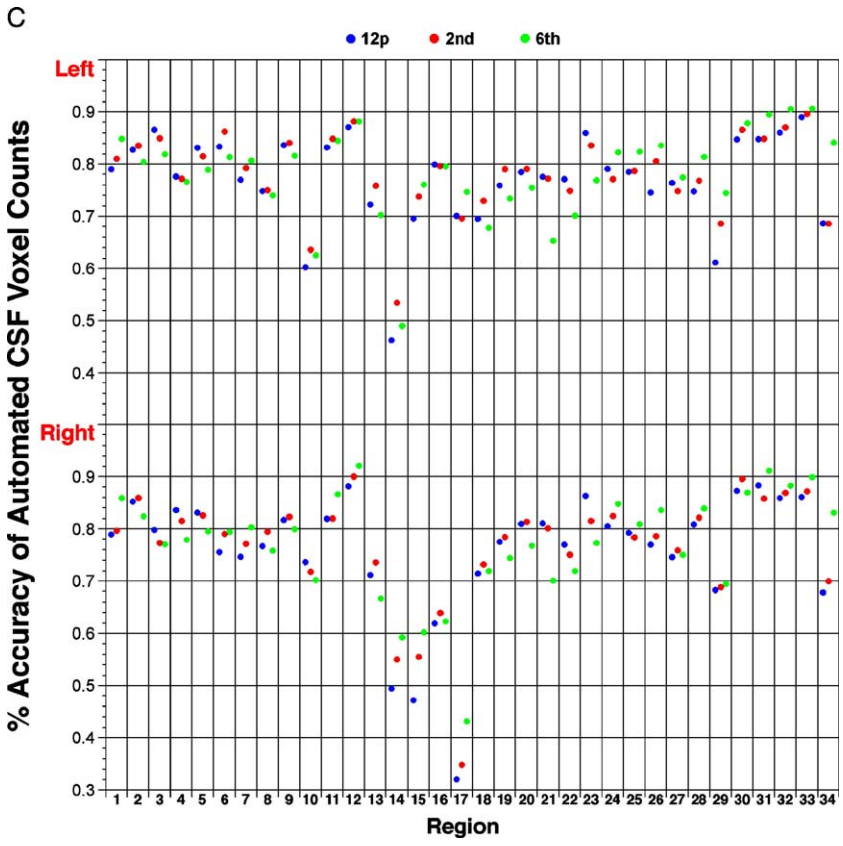

Fig. 2 (*continued*).

with the geometry of its subcortical pattern defined in the atlas target space and then projected down 9-parameter transforms into each subject's native space data. This was necessary to ensure a similar geometry of white matter boundaries across the probability gradients since the subcortical white matter has no distinct anatomical divisions. Once the underlying white matter geometry of adjacent ROIs was defined in each subject's native scans, the manual editing process began tailoring ROIs to each subject's unique cortical anatomy. After all 68 left and right 3D ROI were created, the GM, WM, and CSF tissue maps were used to partition the ROI into their three tissue components. These subdivided ROI where then projected down the 3 registration matrices from subject's native space to the atlas allowing construction of the probability gradients for 12 p, 2nd order, and 6th order SVPAs.

SVPA atlas construction and utilization

Following data co-registration and intensity normalization, as described above, construction of the sub-volume probabilistic atlas consisted of calculating the chance that each voxel within the deterministic atlas-space belongs to any of the 34 ROIs. Together with three different tissue types and two hemispheres for each ROI, this constituted a total of 204 (34 × 3 × 2) sub-volumes of interest (SVI). If P is the tissue type of subject n,

$$P_n^{(v)} = \begin{cases} 0, \text{background} \\ 1, \text{WM} \\ 2, \text{GM} \\ 3, \text{CSF} \end{cases}$$

$1 \le n \le 20$, at voxel location v, $1 \le v \le 5{,}445{,}000$ (=200 × 165 × 165),

$$I_S^{(v)} = \begin{cases} 1, v \in S \\ 0, v \notin S \end{cases}$$

and $I_{\mathrm{ROI}r}^{(v)}$, $1 \le r \le 34$, is the indicator function of the r^{th} ROI of the SVPA, then $P_{n,r}(v) = P_n(v) \times I_{\mathrm{ROI}r}^{(v)}$ represents the tissue type for subject n, at location v, over the r^{th} ROI. Then, the SVPA atlas was

Table 2
Mean left and right % accuracy for the absolute tissue counts and Pearson correlation coefficients for the ratio measures across all 68 sub-volumes across the 20 subjects for both the raw tissue counts and the counts corrected for intracranial volume (ICV)

	12p linear		2nd order		6th order	
	Raw counts	ICV corrected	Raw counts	ICV corrected	Raw counts	ICV corrected
Absolute WM	0.847	0.847	0.855	0.856	0.864	0.864
WM ratio	0.836	0.829	0.860	0.854	0.875	0.869
Absolute GM	0.862	0.863	0.865	0.866	0.864	0.865
GM ratio	0.852	0.845	0.877	0.872	0.886	0.881
Absolute CSF	0.759	0.758	0.772	0.772	0.771	0.771

Note. Absolute cerebral spinal fluid (CSF) counts were used for the ventricles, and absolute gray matter (GM) counts were used for the amygdala, hippocampus, thalamus, subtantia nigra, lenticular, accumbens, and caudate nuclei in all the assessments above.

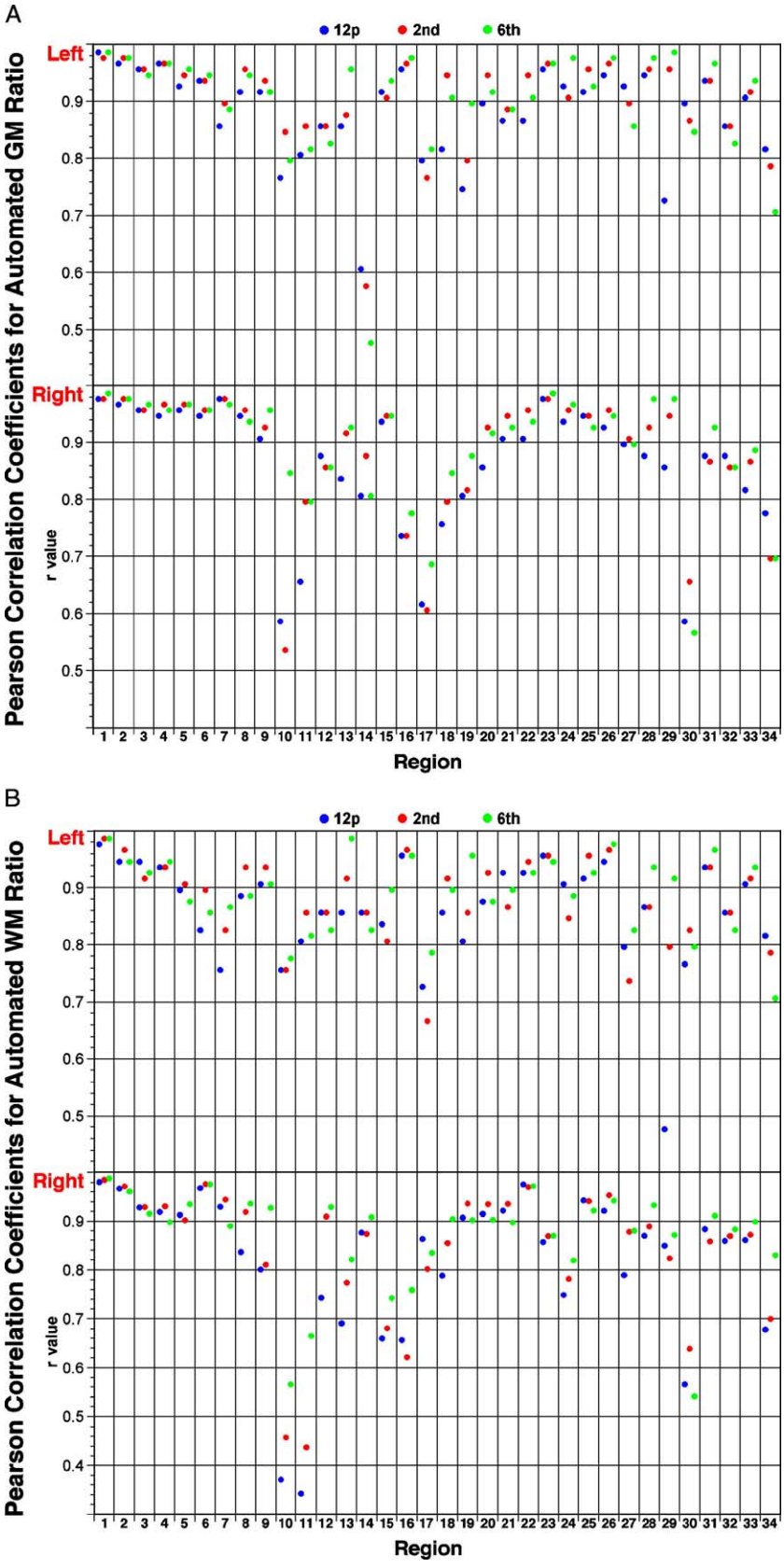

Fig. 3. (A,B) Pearson correlation coefficients for the gray matter (A) and white matter (B) ratios controlling for the amount of CSF in each sub-volume constructed (see text) using three different alignments to the population-based target atlas: 12 parameter affine, 2nd order warp, and 6th order warp. All automated counts were compared against the "gold standard" native-space counts to produce "*r* values" across twenty subjects (see Table 1 for the regions studied). Note: absolute CSF counts used for the ventricles in panels (A) and (B), absolute GM counts used for the hippocampus, amygdala, thalamus, subtantia nigra, lenticular, accumbens, and caudate nuclei in panel (A).

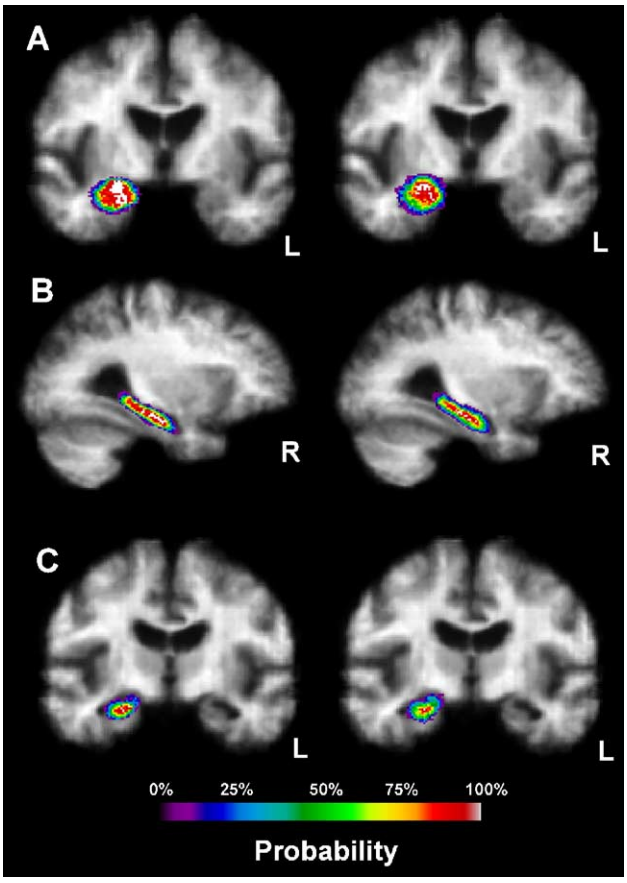

Fig. 4. (A,B,C) Probability gradients for gray matter voxels in medial temporal structures constructed across different registration matrices of the 20 subjects into the atlas. (A) Amygdalar gradients derived from 6th order warps (left) compared to 12 parameter registrations (right). (B and C) Hippocampal gradients derived from 6th order warps (left) compared to 12 parameter (right) registrations.

constructed as a set of 204 volumes SVPA(k) each of which contained the probability maps for one SVI_k:

$$\mathrm{SVPA}(k,v) = \frac{1}{20}\sum_{n=1}^{20} I^{(v)}_{\{L(n,v)=k\}},$$

where $L(n, v) = 102 \times h + 34 \times t + r - 1$ is the numeric SVI label associated with voxel v for subject n, $h = 0, 1$ (left/right hemisphere), $t = 0, 1, 2$ (tissue type), and $1 \leq r \leq 34$. An SVPA value of 1 indicates that the chance this voxel is part of the k^{th} SVI is 100%, whereas a value close to 0 means the voxel is not likely to belong to the k^{th} SVI. This construction yields a 3D volume, SVPA(k, v), for each region in which we count all selected tissue type voxels that fall in the region of interest having 50% or higher chance of belonging to the specified region. Another atlas representation, useful primarily for visualization purposes, is obtained by merging all probabilistic volumes encoding the 204 SVIs into a single 3D volume. This is achieved by subdividing the intensity spectrum of short integers [0, 1, 2,..., 65535] into 204 sectors of equal size and placing the SVPA(k, v) probability maps into the appropriate band. For a fixed voxel location v_o, the intensity of the single atlas volume is defined by

$$\mathrm{SVPA}(v_o) = (k_o - 1)\,(65536) \,/\, (204) + 20 \times \mathrm{SVPA}(k_o, v_o),$$

where

$$k_o = \max_{1 \leq k \leq 204} \{20 \times \mathrm{SVPA}(k, v_o)\}.$$

In practical calculations, however, we used the raw SVPA atlas, which consisted of 204 individual probability volumes, one for each SVI. Since there is significant overlap between some regions, the complete SVPA atlas must be stored as a 204 dimensional vector field over the atlas voxel matrix or (as we did) as 204 individual probabilistic SVI volumes, $\mathrm{SVPA}_k(v)$, $1 \leq k \leq 204$.

The SVPA atlas may also be used to locate structures for any subject automatically by co-registering the deterministic SVPA to a subject's native space brain volume (with global tissue maps) and computing the voxel counts of each tissue type within each of the 204 SVIs in the SVPA atlas. The subject's volume over SVI_k is computed (subject to a specified probability level, P) by $V_k = \sum_v I^{(v)}_{\{P \leq R\_\mathrm{SVPA}_k(v)\}}$, where $R\_\mathrm{SVPA}k(v)$ is the reslice of the kth SVPA region into subject's native space and P is a probability level (P small/large yields a broad/conservative volumetric measure, respectively). In the case of affine registration, one often reslices the atlas volumes in the subject's space. This requires correction of the morphometric measurements by the magnitude of the Jacobian of the affine spatial transformation. On the other hand, when aligning the SVPA to subject space, special care is required

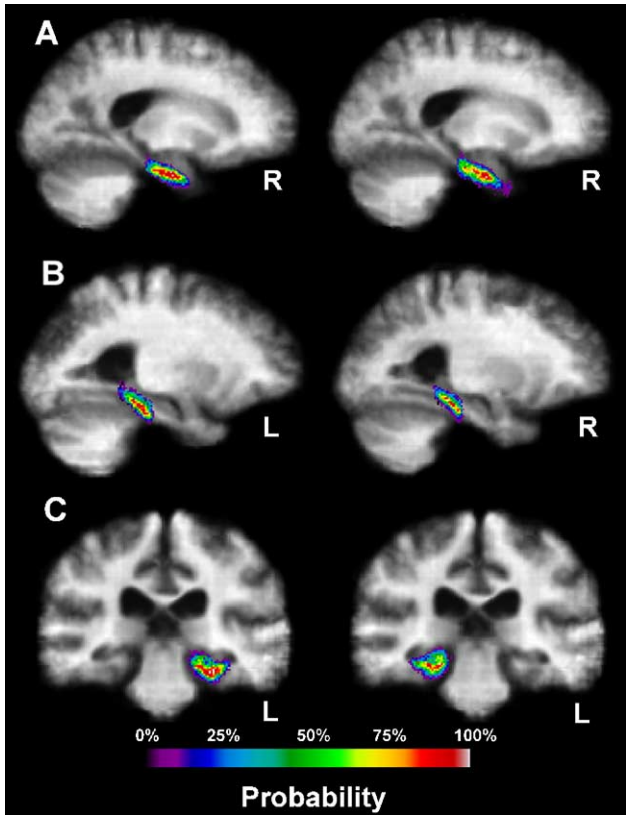

Fig. 5. (A,B,C) Probability gradients for gray matter voxels in medial temporal structures constructed across different registration matrices of the 20 subjects into the atlas. (A) Anterior parahippocampal gradients derived from 6th order warps (left) compared to 2nd order warps (right). (B and C) Posterior parahippocampal gradients derived from 2nd order warps comparing the differential laterality effects in the population.

during the reslicing step to avoid smoothing or altering the atlas SVI label intensities as the latter are critical in volume calculations.

SVPA validation

Determining which of the three constructed SVPAs best calculates tissue voxels, a comparison of automated versus manual "gold standard" ROI voxel counts was preformed using difference measures with a cross-validation "jack-knife" analysis for the 20 subjects. The "jack-knife" procedure avoids the bias of using the same subjects that made up the SVPA probability gradients in testing the SVPA's accuracy. Twenty unique SVPAs for each of the three registration transforms were created with 19 subjects leaving out a single subject whose volumes were assessed by that SVPA they did not contribute toward constructing. Tissue counts corrected for each subject's intracranial volume (ICV) and absolute tissue counts (i.e., GM, WM, and CSF counts not corrected for ICV) were assessed separately. Percent accuracy was computed using difference measures of the automated versus manual voxel counts for the three tissue types (GM, WM, and CSF) across all subjects' sub-volumes using the "jack-knife" constructed SVPAs. Since the automated counts within an SVPA at times compute a larger, and other times, a smaller voxel count than the manual method within native space, we used the absolute value of these difference measures. Because a difference of 100 voxels is more significant in a structure the size of the thalamus than in the entire lateral ventricles, we divided the absolute value of these differences by the total tissue volume found in the manual measures (and subtracted this fraction from 1) to give a "percent accuracy" measure.

Guided from our previous experience with past SVPA construction (Mega et al., 2000), we also evaluated two novel measures: GM and WM ratios ([GM + CSF] / CSF = GM%, and [WM + CSF] / CSF = WM%) for each sub-volume. Because any given probability gradient can count all three tissue types of a subject's scan, these ratios measure reflect atrophy associated with the increasing CSF component within a region. These GM and WM ratios represent a new metric derived from the SVPA's probability gradients and thus are best evaluated with Pearson correlation coefficients (Bland and Altman, 1986) when compared against the deterministic manual ROI tissue ratios in native space.

Results

Figs. 2A,B,C demonstrate accuracy data for the ICV uncorrected (or absolute) tissue counts in the 3 SVPAs compared to the "gold standard" native space counts. Evaluation of the ICV corrected counts showed no advantage over uncorrected counts (see Table 2). Regional gradients constructed from higher order warps often showed superiority to the gradients derived from the linear registrations to the atlas.

Given that the probability gradients constructed from each sub-volume can count all voxels from the GM, WM, and CSF that fall within them in any given subject, the GM ratio and WM ratio counts were also compared to the manually derived ratios (see Figs. 3A,B). Absolute counts were used instead of ratio counts in Figs. 3A,B however when the regions had primarily one tissue type (absolute CSF counts used for the ventricles in A and B, absolute GM counts used for the hippocampus, amygdala, thalamus, subtantia nigra, lenticular, accumbens, and caudate nuclei in A). The mean bilateral GM ratio correlation coefficients for the 3 SVPAs were 0.85 for the 12 p SVPA, 0.88 for the 2nd SVPA, and 0.89 for the 6th SVPA (calculated with the absolute GM and CSF substitutions noted above). The mean bilateral WM ratio correlation coefficients for the 3 SVPAs were 0.84 for the 12 p SVPA, 0.86 for the 2nd SVPA, and 0.88 for the 6th SVPA (calculated with the absolute GM and CSF substitutions noted above).

Visual inspection of the probability gradients constructed from the three different registration matrices reveals the population's anatomical variability and how that variability is controlled across high and low polynomial registrations as shown for the medial temporal regions in Figs. 4A,B,C. Right-sided variability of the amygdala and hippocampus is controlled better with 6th order warps compared to 12 parameter linear registrations (also see Fig. 3A for "r values" derived in the ratio counts from these regional gradients).

Given that the parahippocampal gyrus is an area of interest for imaging in aging and dementia, its variability deserves attention (see Figs. 5A,B,C). Although 6th order warping improved the GM ratio over the 2nd order and 12 parameter registrations for the right anterior parahippocampus, it did not do so on the left where 2nd order warping was superior in both GM ratio and accuracy. In the posterior parahippocampus, 2nd order warping was also superior in GM accuracy measures bilaterally but not in GM ratio measures.

Discussion

We sought to develop an imaging assessment tool that achieved the following goals: (1) The imaging tool must control for anatomic variability and registration errors produced when comparing datasets in a common coordinate system. We chose a Talairach compatible coordinate system constructed from a population most similar to that found in clinics evaluating dementia patients as our "target atlas space" (Thompson et al., 2000a,b, 2001a,b). The "ideal" SVPA within this target space is somewhat regionally dependent but in general the higher order 2nd and 6th SVPAs outperformed the 12p SVPA in controlling anatomic variability and registration errors. The increased processing time necessary for the higher order warps (30 min versus 5 min when run on a G4 processor on the McIntosh OS10.2 platform) might outweigh the 4% improvement of the automated assessment tool (average r = 0.89 for 6th SVPA versus 0.85 for the 12p SVPA).

(2) The imaging tool must allow for regionally testable hypotheses. This imaging tool allows for such diverse regionally selected brain analysis given the 204 sub-volumes embedded in each SVPA. (3) To ensure inter-center application, the imaging strategy must be automated, freely available, and not require extensive computer resources. We present here an automated imaging tool that uses freely available software packages compiled on a G4 McIntosh running OS10.2 (email the author for the terms of its use). The time savings for an automated multi-regional assessment tool over manual region delineation are enormous. The manual region generation for the 20 datasets used to construct the probabilistic atlas described here took over 3000 man-hours to generate. Compared to the roughly 15 h of processing time and 1 h of visualization of registration accuracy, this automated assessment allows a profound time savings. (4) The imaging tool should accommodate growth in its population data. Use of this tool will provide regional tissue counts for an individual subject with the standard deviation each count has within a larger population. This population will increase in size as the number of subjects measured by it increases. The population distribution data will be made

available to the users of this assessment method contingent upon their sharing of their data with other users as is now the goal of the AD Neuroimaging Initiative (ADNI). Only through open sharing of similar assessment tools and longitudinal populations can sufficient statistical power be achieved to evaluate individual patients against the population. Thus, future studies using the ADNI database can test the predictive power of this and other assessment tools in identifying incipient AD within the elderly population.

Variability in the accuracy of the three registration techniques in producing automated tissue volumes, compared to the manual outlines, is driven by two main factors: (1) error in the intensity-based registration algorithms and (2) the inherent variability in brain morphology across a population. Where there is clear intensity interfaces defining a structure's boundary (CSF-GM boundaries) as with the right amygdala, the higher order warp better controls for the morphologic variability of the population (see Fig. 4A) and thus improves accuracy. In parietal and frontal cortices, 12p linear registration is often superior to the higher order warps in GM accuracy measures (and in GM ratio measures for the caudate and temporal pole) perhaps due to inappropriate distortion of brain anatomy by the higher order warp, which AIR has no control over, in a region of homogenous intensity. The choice of which registration method to use should be driven by the hierarchy of regions targeted by a given experiment's hypothesis, thus there is no best overall approach. For these, relatively large ROI structure size does not influence volumetric accuracy of the automated assessment method given the divergent results among similarly sized smaller subcortical (e.g. medulla vs. pons) and larger cortical regions (e.g. left sub-callosal frontal vs. left caudal anterior cingulate) supporting the influence of anatomic variability as a leading contributor of automated volumetric inaccuracy. However, as voxel size becomes larger relative to structure size, all methods using quantified grids eventually break down and variances grow.

Some problems with this current study are that no information on various pulse sequences is provided, thus multi-center data employing different acquisition techniques from differing scanners could produce accuracy results that deviate from those data provided here. Another confound is that found in the potential variation of the segmentation algorithms that may be employed by different centers who choose to use this tool. The accuracy data we describe here assume that the use of a specific segmentation algorithm (Zijdenbos and Dawant, 1994) others employed may change the tissue maps reflected in the regional probability gradients. Future work on this assessment technique will aim to evaluate the diagnostic utility of the ratio measures versus the absolute voxel counts and to construct separate gradients for functional imaging data and incorporate them into the sub-volume thresholding (SVT) assessment (Dinov et al., 2000).

Acknowledgments

Support for this work was provided, in part, by the Brain Mapping Medical Research Organization, Brain Mapping Support Foundation, Pierson-Lovelace Foundation, The Ahmanson Foundation, Tamkin Foundation, Jennifer Jones-Simon Foundation, Capital Group Companies Charitable Foundation, Robson Family, William M. and Linda R. Dietel Philanthropic Fund at the Northern Piedmont Community Foundation, Northstar Fund, and the National Center for Research Resources grants RR12169, RR13642, and RR08655k, the NLM/NIA research grant R01 LM005639, and the NCRR resource grant P41 RR013642.

References

Amunts, K., Malikovic, A., Mohlberg, H., Schormann, T., Zilles, K., 2000. Brodmann's areas 17 and 18 brought into stereotaxic space—where and how variable? NeuroImage 11, 66–84.

Bland, J.M., Altman, D.G., 1986. Statistical methods for assessing agreement between two methods of clinical measurement. Lancet 1 (8476), 307–310.

Chiavaras, M.M., LeGoualher, G., Evans, A.C., Petrides, M., 2001. Three-dimensional probabilistic atlas of the human orbitofrontal sulci in standardized stereotaxic space. NeuroImage 13, 479–496.

Crespo-Facorro, B., Kim, J.-J., Andreasen, N.C., et al., 1999. Human frontal cortex: an MRI-based parcellation method. NeuroImage 10, 500–519.

Dinov, I.D., Mega, M.S., Thompson, P.M., et al., 2000. Analyzing functional brain images in a probabilistic atlas: a validation of sub-volume thresholding. J. Comput. Assist. Tomogr. 24, 128–138.

Folstein, M.F., Folstein, S.E., McHugh, P.R., 1975. "Mini-mental state": a practical method for grading the mental state of patients for the clinician. J. Psychiatr. Res. 12, 189–198.

Geyer, S., Schormann, T., Mohlberg, H., Zilles, K., 2000. Areas 3a, 3b, and 1 of human primary somatosensory cortex2. Spatial normalization to standard anatomical space. NeuroImage 11, 684–696.

Hayashi, K.M., Thompson, P.M., Mega, M.S., Zoumalan, C.I., 2002. Medial hemispheric surface gyral pattern delineation in 3D: surface curve protocol (http://www.loni.ucla.edu/khayashi/Public/medial_surface/MedialLinesProtocol). In: 2002.

Kim, J.-J., Crespo-Facorro, B., Andreasen, N.C., et.al, 2000. An MRI-based parcellation method for the temporal lobe. NeuroImage 11, 271–288.

Leonard, C.M., 1996. Structural variation in the developing and mature cerebral cortex: noise or signal? In: Thatcher, R.W., Reid, L.G., Rumsey, J., Krasnegor, N. (Eds.), Developmental Neuroimaging: Mapping the Development of Brain and Behavior. Academic Press, New York, pp. 207–231.

MacDonald, D., Kabani, N., Avis, D., Evans, A.C., 2000. Automated 3-D extraction of inner and outer surfaces of cerebral cortex from MRI. NeuroImage 12, 340–356.

McKhann, G., Drachman, D., Folstein, M., Katzman, R., Price, D., Stadlan, E.M., 1984. Clinical diagnosis of Alzheimer's disease: report of the NINCDS-ADRDA Work Group, Department of Health and Human Services Task Force on Alzheimer's Disease. Neurology 34, 939–944.

Mega, M.S., Thompson, P.M., Cummings, J.L., Toga, A.W., 2000. The UCLA Alzheimer's disease atlas project: structural and functional applications. Ann. Neurol. 48, 427.

Ono, M., Kubik, S., Abernathey, C.D., 1990. Atlas of the Cerebral Sulci. Georg Thieme Verlag, Stuttgart.

Petersen, R.C., Smith, G.E., Waring, S.C., Ivnik, R.J., Tangalos, E.G., Kokmen, E., 1999. Mild cognitive impairment: clinical characterization and outcome. Arch. Neurol. 56, 303–308.

Sastre-Janer, F.A., Regis, J., Belin, P., et al., 1998. Three-dimensional reconstruction of the human central sulcus reveals a morphological correlate of the hand area. Cereb. Cortex 8, 641–647.

Sled, J.G., Zijdenbos, A.P., Evans, A.C., 1998. A nonparametric method for automatic correction of intensity nonuniformity in MRI data. IEEE Trans. Med. Imag. 17, 87–97.

Sowell, E.R., Thompson, P.M., Holmes, C.J., Jernigan, T.L., Toga, A.W., 1999. Progression of structural changes in the human brain during the first three decades of life: in vivo evidence for post-adolescent frontal and striatal maturation. Nat. Neurosci. 2, 859–861.

Sowell, E.R., Thompson, P.M., Mega, M.S., Zoumalan, C.I., Lindshield,

C., Rex, D.E., 2000. Gyral pattern delineation in 3D: surface curve protocol. http://www.loni.ucla.edu/_esowell/new_sulcvar.html.

Sowell, E.R., Thompson, P.M., Tessner, K.D., Toga, A.W., 2001. Accelerated brain growth and cortical gray matter thinning are inversely related during post-adolescent frontal lobe maturation. J. Neurosci. 21, 8819–8829.

Steinmetz, H., Furst, G., Freund, H.-J., 1990. Variation of perisylvian and calcarine anatomic landmarks within stereotaxic proportional coordinates. Am. J. Neuroradiol. 11, 1123–1130.

Thompson, P.M., Mega, M.S., Toga, A.W., 2000a. Disease-specific probabilistic brain atlases. In: IEEE (Ed.), Proceedings of the International Conference on Computer Vision and Pattern Recognition, and Workshop on Mathematical Methods in Biomedical Image Analysis, pp. 234–237.

Thompson, P.M., Woods, R.P., Mega, M.S., Toga, A.W., 2000b. Mathematical and computational challenges in creating deformable and probabilistic atlases of the human brain. Hum. Brain Mapp. 9, 81–92.

Thompson, P.M., Mega, M.S., Vidal, C., Rapoport, J.L., Toga, A.W., 2001a. Detecting disease-specific patterns of brain structure using cortical pattern matching and a population-based probabilistic brain atlas. In: Insana, M., Leahy, R. (Eds.), IEEE Conference on Information Processing in Medical Imaging. Springer, Davis, CA, pp. 488–501.

Thompson, P.M., Mega, M.S., Woods, R.P., et al., 2001b. Cortical change in Alzheimer's disease detected with a disease-specific population-based brain atlas. Cereb. Cortex 11, 1–16.

White, L.E., Andrews, T.J., Hulette, C., et al., 1997. Structure of the human sensorimotor system. I: Morphology and cytoarchitecture of the central sulcus. Cereb. Cortex 7, 18–30.

Woods, R.P., Grafton, S.T., Watson, J.D.G., Sicotte, N.L., Mazziotta, J.C., 1998. Automated image registration: II. Intersubject validation of linear and nonlinear models. J. Comput. Assist. Tomogr. 22, 153–165.

Zijdenbos, A.P., Dawant, B.M., 1994. Brain segmentation and white matter lesion detection in MR images. Crit. Rev. Biomed. Eng. 22, 401–465.